Asymmetric interaction of a solar wind reconnecting current sheet and its magnetic hole with Earth's bow shock and magnetosphere

Hadi Madanian[1], Terry Zixu Liu[2], Tai-Duc Phan[3], Karlheinz Trattner[4], Tomas Karlsson[5], and Michael W. Liemohn[6]

[1]Southwest Research Institute
[2]University Corporation for Atmospheric Research
[3]UC Berkeley
[4]Laboratory for Atmospheric and Space Physics
[5]KTH Royal Institute of Technology
[6]University of Michigan-Ann Arbor

November 22, 2022

Abstract

We report results of our analysis of a solar wind reconnecting current sheet (RCS) and its solar wind magnetic hole observed on 20 November 2018. In the solar wind, the normal vector to the current sheet plane makes an angle of 32° with the Sun-Earth line. A combination of tilted current sheet plane and foreshock effects cause an asymmetric interaction with the bow shock, such that the structure arrives at the quasi-perpendicular side of the bow shock before the quasi-parallel side. The solar wind flow slowdown and deflection during the bow shock crossing significantly disrupt the reconnection exhausts within the RCS. Unlike localized magnetosheath jets, the solar wind RCS has a global impact on the bow shock and the magnetopause. Plasma flow deflection in the magnetosheath also increases with the passage of the RCS. The magnetic field strength inside the magnetic hole decreases by ˜69 percent in the solar wind, with a similar depression rate observed inside the magnetosheath due to this structure. The ion density and temperature both increase within the current sheet to form a roughly pressure balanced structure. Field rotation and change in the dynamic pressure during this event modify the reconnection zones at the magnetopause and cause an inward motion of this boundary.

Asymmetric interaction of a solar wind reconnecting current sheet and its magnetic hole with Earth's bow shock and magnetosphere

Hadi Madanian[1], Terry Z. Liu[2], Tai D. Phan[3], Karlheinz J. Trattner[4], Tomas Karlsson[5], Michael W. Liemohn[6]

[1]Southwest Research Institute, San Antonio, TX, USA
[2]University of California Los Angeles, Los Angeles, CA, USA
[3]Space Sciences Laboratory, University of California, Berkeley, CA, USA
[4]Laboratory for Atmospheric and Space Sciences, Boulder, CO, USA
[5]KTH Royal Institute of Technology, Stockholm, Sweden
[6]Department of Climate and Space Sciences and Engineering, University of Michigan, Ann Arbor, MI, USA

Key Points:

- Solar wind RCS are large-scale structures that asymmetrically interact with the bow shock and the magnetopause.
- Higher plasma heating and ion flow deflection are observed within the shocked RCS plasma.
- RCS and SWMH modulate the reconnection process at the magnetopause and cause deformation of the boundary.

Corresponding author: Hadi Madanian, `hmadanian@gmail.com`

Abstract

We report results of our analysis of a solar wind reconnecting current sheet (RCS) and its solar wind magnetic hole observed on 20 November 2018. In the solar wind, the normal vector to the current sheet plane makes an angle of 32° with the Sun-Earth line. A combination of tilted current sheet plane and foreshock effects cause an asymmetric interaction with the bow shock, such that the structure arrives at the quasi-perpendicular side of the bow shock before the quasi-parallel side. The solar wind flow slowdown and deflection during the bow shock crossing significantly disrupt the reconnection exhausts within the RCS. Unlike localized magnetosheath jets, the solar wind RCS has a global impact on the bow shock and the magnetopause. Plasma flow deflection in the magnetosheath also increases with the passage of the RCS. The magnetic field strength inside the magnetic hole decreases by ∼69 percent in the solar wind, with a similar depression rate observed inside the magnetosheath due to this structure. The ion density and temperature both increase within the current sheet to form a roughly pressure balanced structure. Field rotation and change in the dynamic pressure during this event modify the reconnection zones at the magnetopause and cause an inward motion of this boundary.

Plain Language Summary

Space Weather is the study of effects of solar inputs on on the space environment surrounding Earth. A source of solar input is through the solar wind, a stream of charged particles from the Sun carrying the interplanetary magnetic field. In this study, we analyze effects of a particular type of solar wind anomaly on Earth. The structure is initially observed by solar wind monitors far upstream of Earth, and later appears in the data of several near Earth spacecraft. We show that the structure can pass through the outer most boundary around Earth, the bow shock, and propagate closer to Earth. This study has significance in shaping our understanding of space weather as it describes near-Earth effects of a commonly observed solar wind phenomenon.

1 Introduction

Reconnection has been widely studied and observed in various space plasma environments such as solar flares, the solar wind, Earth's magnetotail and magnetopause (Gosling, 2012; Paschmann et al., 2013; Hesse & Cassak, 2020; Khotyaintsev et al., 2019; Treumann & Baumjohann, 2013; Yamada et al., 2010; Zweibel & Yamada, 2016, & references therein). During reconnection, the magnetic field morphology at the intersection of two rather different plasma environments change in order to diffuse the energy of opposing flows. In the solar wind, a reconnecting current sheet (RCS) is characterized by a rotation in the IMF accompanied by Alfvénic accelerated plasma flows also known as reconnection exhausts (Gosling et al., 2005). Alfvénic disturbances generated during reconnection propagate along reconnected magnetic field lines and accelerate and heat the plasma along their way. For a spacecraft that is relatively stationary in the supersonic solar wind flow, such a structure will appear as correlated changes in the magnetic field ($\mathbf{B}$) and the plasma velocity ($\mathbf{V}$) on one side, and anti-correlated changes on the other side of the reconnection exhaust. The current sheet can appear as back-to-back rotational discontinuities (i.e., a bifurcated current sheet) or as a single current sheet (Phan et al., 2006; Gosling & Szabo, 2008; Phan et al., 2009). The physical processes that initiate reconnection are not well determined. A few models describe the scaling relation between plasma parameters during reconnection (Cassak & Shay, 2007; Petschek, 1964; Parker, 1957). Theoretical studies suggest that in the solar wind, compression of the sectored solar wind flow can lead to reconnection (Drake et al., 2017). Reconnection can also be initiated spontaneously. Transfer of magnetic energy to particles creates a magnetic depression or a magnetic hole at the reconnection site. The level of depression varies with distance to the X-line of an expanding exhaust. Energy release during reconnection is also a source of free energy that drives further plasma instabilities causing turbulence in the magnetic field and plasma flow near the reconnection zone (Osman et al., 2014).

Interaction of transient solar wind structures with Earth's bow shock and magnetosphere has been the topic of many investigations. It has been shown that sudden changes in the IMF direction across rotational discontinuities (RDs) can alter the energy input and reconnection rate at the magnetopause, and modify the solar wind - magnetosphere - ionosphere coupling (Andreeova et al., 2011; Liemohn & Welling, 2016; Tsurutani et al., 2011). Archer et al. (2012) showed that some RDs transfer into the magnetosheath in the form of pressure pulsations. Transition of the shock geometry from quasi-perpendicular to quasi-parallel allows the formation of high-pressure plasma parcels at certain regions downstream of the shock. Conventionally, magnetosheath "high-speed" jets are known to have a characteristically high velocity component along the magnetopause normal vector that gives rise to the enhanced dynamic pressure (Escoubet et al., 2020; Hietala & Plaschke, 2013; Plaschke et al., 2013). High plasma density anomalies in the magnetosheath can also produce high dynamic pressure magnetosheath structures (Blanco-Cano et al., 2020). It has also been shown that compression of the current sheet across solar wind discontinuities at the bow shock can initiate reconnection (Lin, 1997; Phan et al., 2007; Hamrin et al., 2019), as does the compression of current sheets at the magnetopause (Hietala et al., 2018; Phan et al., 2011). Current sheet thinning, high magnetic shear angle, and low $\Delta\beta$ are favorable conditions for reconnection (Paschmann et al., 1982; Phan et al., 2010).

Bow shock and foreshock environments also significantly modify the current density within RDs (Kropotina et al., 2021). Crossing the bow shock can also disrupt the reconnection exhausts and shut off the reconnection process within the RCS (Phan et al., 2011). In some cases, density increase within upstream discontinuities generates a fast shock that propagates in front of the discontinuity in the magnetosheath (Maynard et al., 2008). Due to pressure variations and rarefaction effects, interplanetary shocks induce a rocking motion in the bow shock layer when they cross it (Šafránková et al., 2007). Once inside the magnetosheath, interplanetary shocks take the form of a discontinuity (Zhang et al., 2009). Bow shock crossing also significantly modifies the structure of magnetic clouds, plasma events associated with interplanetary coronal mass ejections and characterized by enhancements in the magnetic field strength during slow field rotations (Farrugia et al., 1995; Turc et al., 2016). Another widely observed solar wind transient phenomena are magnetic holes (MHs) (Turner et al., 1977), characterized as sudden decreases in the magnetic field strength in an otherwise unperturbed solar wind flow. Depending on the level of magnetic field rotation across the depression, solar wind magnetic holes (SWMHs) are typically classified as linear or rotational holes (Turner et al., 1977; Volwerk et al., 2021). These pressure-balanced structures have been observed at various heliocentric distances and plasma environments and can appear in different size scales (Burlaga et al., 1990; Karlsson et al., 2021; Madanian et al., 2020; Sperveslage et al., 2000; Wang et al., 2020). SWMHs can bypass the bow shock almost intact and appear in the magnetosheath plasma as a high momentum plasma parcel (Karlsson et al., 2015, 2016). Generation mechanism of MHs has been a point of debate (Tsurutani et al., 2011). Several studies have determined that linear holes are associated with mirror mode waves in high beta plasmas (Burlaga et al., 2007; Balikhin et al., 2012; Volwerk et al., 2021).

In this paper we analyze the interaction of a RCS and its associated SWMH with Earth's bow shock and magnetosphere using a combination of multi spacecraft data and a convection model. Given the relatively high occurrence rate of RCSs, it is important to have a better understanding of their impacts on Earth's magnetosphere. In Section 2, details of observations at several plasma boundaries and environments are shown. Discussions of results are provided in Section 3, and the paper is concluded in Section 4.

2 Observations

We use data from the Advanced Composition Analyzer (ACE) (Stone et al., 1998), Wind (Harten & Clark, 1995), Cluster (Escoubet et al., 2001), Time History of Events and Macroscale Interactions during Substorms (THEMIS) (Angelopoulos, 2008), and the Magnetospheric Multiscale (MMS) (Burch et al., 2016) missions. For the Cluster constellation, plasma data are only available from Cluster4 during the event studied here. Also, Cluster3 and 4 spacecraft travel similar orbits and make nearly identical measurements. As such, Cluster3 data will not be discussed. Similarly, the four MMS spacecraft are in a close tetrahedron formation (less than 20 km intra-spacecraft separation) during this event, and we limit our discussion to data from satellite 1 (MMS1). The structure size and the dynamics scales being analyzed in this study are larger than the spacecraft separation spatial and temporal scales, and therefore small kinetic-scale differences between the MMS spacecraft observations are not needed for this study. The arrangement of spacecraft provides a relatively good coverage of dayside Geospace, allowing for a more thorough analysis of the nature of the upstream RCS interaction with Earth's magnetosphere. All vector quantities in the paper are expressed in the geocentric solar magnetic (GSM) coordinate system in which the X–axis points towards the Sun, the Y–axis is perpendicular to Earth's magnetic dipole axis, and Z completes the right-hand triple.

2.1 RCS in the solar wind

The RCS is initially observed by two solar wind monitors at Lagrange point 1. Panels (a) and (b) in Figure 1 show the IMF profile measured by ACE and Wind spacecraft, respectively, for a time interval between 07:50:00 and 09:30:00 UT on 20 November 2018. The ACE spacecraft is at (239.1, -15.9, 26.5) R_E (R_E = Earth radius), while the Wind spacecraft is downstream from ACE at (195.7, -29.2, 7.7) R_E. Comparing the two time series, there are a few magnetic depressions at the beginning of the interval in ACE data which seem to have been replenished during the transport to Wind. We focus on the magnetic hole structure in the middle of the interval in panel (a) between 08:31:28 and 08:35:24 UT. Throughout this paper, we consider the field rotation/reversal due to the RCS occurring throughout the entire SWMH period as a single structure and refer to it as the "structure" or the RCS. The magnetic field depression ratio is defined as $\delta B = |B_{in} - B_{out}|/B_{out}$, where B_{in} and B_{out} are the average field strength inside and outside the SWMH, respectively. ACE measures a δB of 0.50 for this structure. A very similar and comparable depression ratio of 0.57 is seen in Wind data between 08:39:14 and 08:48:25 UT, corresponding to the same structure transported by the solar wind. However, the magnetic field strength inside the magnetic hole drops to lower values in Wind data compared to ACE.

For the highlighted interval in panel (b) we show the magnetic field and bulk plasma flow velocity components measured by Wind in panels c–e. The boundaries (vertical dashed lines) are determined at times when there is a significant change in the magnetic field strength and orientation. The leading edge of the structure is characterized by a fast rotation of the field and a simultaneous decrease in the field strength. The event duration also increases from 236 s at ACE to more than double ∼551 s at Wind. This expansion is either indicative of dynamic plasma processes within the structure that have widened the current sheet, or different spacecraft distances to the X-line of an expanding exhaust. Nevertheless, the RCS and its SWMH is a magnetohydrodynamic scale structure (above electron and proton kinetic scales).

Panels c–e in Figure 1 show magnetic field and plasma flow velocity components from Wind measurements. At the leading edge of the current sheet, field rotation occurs through rapid changes in all three components of the magnetic field, but variations extend rotation period and approach the post current sheet values at different rates. These

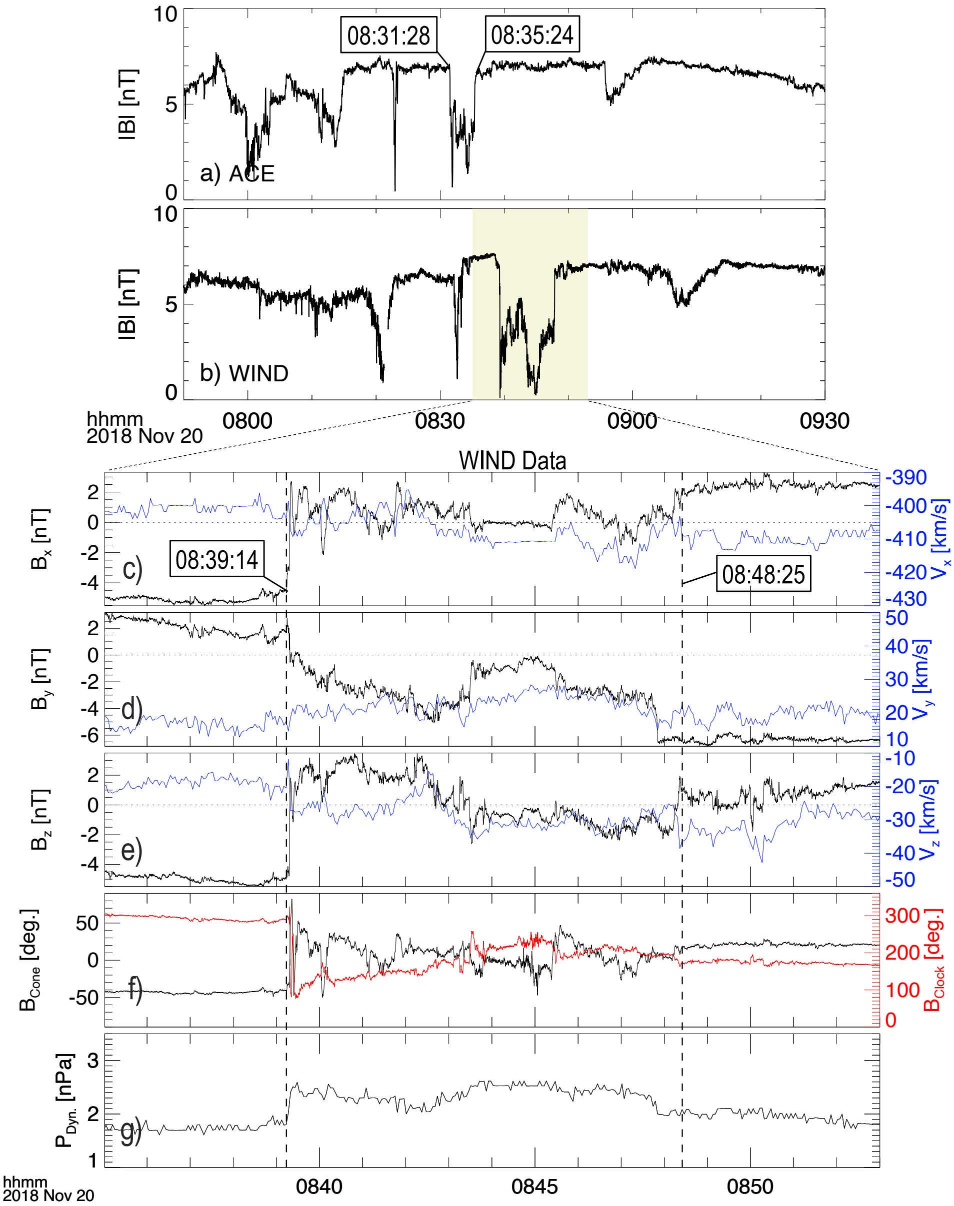

Figure 1. Solar wind magnetic field, flow velocity, and dynamic pressure for an RCS on 20 November 2018. Panels (a) and (b) show the IMF strength measured by ACE and Wind spacecraft, respectively. Panels (c–e) show GSM components of the magnetic field in black and the flow velocity in blue measured by Wind for the highlighted interval in panel (b). Panel (f) shows the magnetic field clock angle in red and the cone angle in black, and the dynamic pressure is shown in panel (g). The RCS and its SWMH boundaries are marked with time tags in panel (a) for ACE data, and with vertical dashed lines in panels (c–g) for Wind data.

rotations are evident in the magnetic field cone ($arcsin(B_x/|B|)$) and clock ($arctan(B_z, B_y)$) angles in Figure 1.f. A cone angle of 0° indicates an IMF vector in the plane perpendicular to the Sun–Earth line. In that plane, the clock angle is measured from the +Y–axis and varies in the $0 - 2\pi$ range. Before the crossing of the current sheet, the IMF has a cone angle $\sim 42°$ and clock angle $\sim 289°$. Immediately after the field rotation at 08:39:12

UT, the cone and clock angles change to $\sim$ 35° and 126°, respectively. Note that the clock angle continues to increase inside the magnetic hole. On the trailing edge, the IMF strength returns to pristine solar wind values mainly through an increase in B_y and B_x components, and the cone angle approaches to 20° and the clock angle remains at 176°. The magnetic shear angle (α) across the structure is 119.6° at ACE which slightly reduces to 118° at Wind.

The structure also appears to be bifurcated, as commonly observed in RCSs, with field components plateaued near its center. We also observe correlated/anti-correlated changes in **V** and **B** are best seen along the Y component in panel (d). Subtle changes in the flow velocity ($\sim$15 kms^{-1} from the background solar wind) are most likely due to the reconnection exhaust. There are also velocity variations in the X and Z components but it is difficult to discern clear correlated/anti-correlated effects. The local Alfvén speed is relatively low ($\sim$ 20kms^{-1}). In addition, there are also other dynamic plasma processes at play driving the plasma. Figure 1.g shows the increase in the solar wind dynamic pressure ($P_{dyn.} = \rho v^2$, where ρ is the plasma mass density and v is the flow speed). Inside the magnetic hole, the plasma density increases from 6.4 to 8.5 cm^{-3} and the plasma temperature rises from 7.7 to 12.4 eV. These observations are consistent with an extended RCS in the solar wind. Electron distributions (not shown) measured by Wind showed that strahl electrons are absent inside the magnetic hole, but they are observed at near 180° pitch angles after the event when B_x turns positive, and also before the series of disturbances that preceded the event. At no instance are strahl electrons observed parallel to the magnetic field line, even when B_x is negative, which eliminates the possibility of observing magnetic holes during heliospheric current sheet crossings (Kahler & Lin, 1994; Maynard et al., 2011).

The normal vector to the RCS plane obtained from the minimum variance analysis (MVA) of the Wind magnetic field data is $n_{cs} = (-0.84, -0.26, 0.45)$. The normal vector at ACE deviates from this vector by less than 8°. This difference could be due to rotation of the plane phase, or uncertainties associated with applying the MVA. Nonetheless, the large ratio of intermediate to minimum eigenvalues of the variation matrix, and small field variations along the minimum variance direction suggest that the MVA results are reliable and the normal vector is determined reasonably well. Figure S1 in Supplementary Information shows more details of the MVA.

ACE and Wind spacecraft are $\sim$ 50 R_E apart during this event, mostly along the Sun-Earth line. Spacecraft positions are listed in Table 1. Based on the solar wind bulk flow velocity and the RCS normal vector, the expected travel time between the two spacecraft is 420 s which is within 10% of the time lag (466 s) of observations of the leading edge of the RCS (see Table 1). The distinct change in the clock angle, the intense reduction of the magnetic field strength, and the simultaneous increase in density and dynamic pressure enable distinguishing and tracking the structure through different environments and spacecraft datasets. In addition, on either side of the structure the solar wind plasma remains calm and steady for more than five minutes which reduces the amount of turbulence and interference at the bow shock and in the magnetosheath, thereby simplifying the interpretation of time series data.

2.2 Arrival at the bow shock

At around 09:32:00 UT (corresponding to a $\sim$53 minute transition time to the nose of the bow shock from L1), several Earth-orbiting spacecraft are spread across the dayside bow shock, magnetosheath, and magnetopause. Figure 2 shows trajectories of THEMIS, Cluster and MMS spacecraft projected on XY (left) and XZ (right) planes of the GSM coordinates for a three-hour interval starting at 09:30:00 UT. Before the SWMH arrives at the bow shock, the MMS spacecraft are on an inbound trajectory in the magnetosheath, having just crossed the bow shock. THD and THE spacecraft are in the solar wind and near the nose of the bow shock, while THA is inside the magnetosheath and closer to the magnetopause boundary. Cluster1, 2, and 4 spacecraft are inside the magnetosphere boundary layer, with Cluster1 being closest to the boundary at the dusk flank side. In Figure 2, we also show modeled magnetopause (solid lines) and bow shock (dashed lines) boundaries for two sets of upstream conditions. The model parameters including Alfvénic Mach number ($M_{Alf.}$), the solar wind dynamic pressure ($P_{dyn.}$), and the B_z component of the IMF are annotated on the left panel. The grey lines show boundaries standoff distance for conditions inside the magnetic hole (grey parameters).

Figure 3 shows an overview of plasma and field data from MMS1. The magnetic field data are provided by the magnetometer system (Russell et al., 2016), and the plasma is probed by the Fast Plasma Investigation (FPI) instrument (Pollock et al., 2016). MMS initially crossed the bow shock at 09:28:45 UT, 75 s earlier before the plotted interval. Significant wave activities were observed in the shock foot at that time with properties similar to whistler mode precursor waves (Fairfield, 1974). The spacecraft is initially in the magnetosheath but it emerges to the upstream solar wind as the RCS hits the bow shock.

The magnetic field rotation at the leading edge of the RCS is observed by MMS inside the magnetosheath at 09:32:19 UT. The rotation is followed by a significant decrease in the magnetic field strength data which corresponds to the shocked SWMH plasma. MMS remained inside the magnetosheath for another 140 s before the bow shock layer retreats passed the spacecraft position. Figure!3.c shows the electron energy spectrogram and heated solar wind plasma inside the magnetosheath. The heating rate of the solar wind in the magnetosheath increases in the transited magnetic hole. Note the clock angle change from 275° to ∼160° at the leading edge of the RCS. Across the magnetic hole, both inside and outside the magnetosheath, the cone and clock angles in general show similar patterns to those in the solar wind upstream of the bow shock, although there are more perturbations in the magnetic field inside the magnetosheath. The bulk plasma velocity components shown in panel (d) indicate that the solar wind slowdown along the X–axis and deflection along the Y–axis are dominant effects downstream of the bow shock. The solar wind reconnection exhausts are obscured in the sheath plasma. There are slight differences in the flow velocity in the magnetosheath between the onset of the field rotation and the bow shock crossing at ∼09:34:38 UT. For instance, V_y decreases by about ∼17 kms^{-1} from 160 to 143 kms^{-1}. Similar variations also exist in V_z. These small changes are superimposed on the flow deflection and slowdown incurred by the bow shock, though

Table 1. Properties of the SWMH observed by different spacecraft

Region*	source	$\alpha(°)$	δB	$n^{\dagger}$(cm^{-3})	δt(s)	t_i	t_f	$\beta^{\dagger}$	$V^{\dagger}_{Alf.}$(kms^{-1})	$r_{GSM}(R_E)$
SW	ACE$^+$	119.6	0.5	5.4(-)	236	8:31:28	8:35:24	5.2(0.48)	32.8(67.4)	(239.7, -15.9, 26.5)
	WIND	118.2	0.69	8.7(6.6)	551	8:39:14	8:48:25	22(1)	22.6(64.9)	(195.7, -29.9, 7.6)
BSh	MMS		0.49	11.5(9.8)	302	9:32:42	9:37:44	20.6(4.2)	23(47.1)	(3.9, 21.1, -2.8)
	THD‡	122.3	0.67	-	274	9:33:07	9:37:42	-	-	(11.8, -3.4. 5.9)
	THE‡		0.67	-	272	9:33:23	9:37:55	-	-	(11.1, -5.1, 6.3)
MSh	THA	103.2	0.7	37.4(27.5)	335	9:35:27	9:41:03	47.1(2.8)	38.8(125.3)	(9.0, -3.7, 5.8)

*SW: Solar wind, BSh: Bow shock, MSh: Magnetosheath

†Values in () are measured outside the magnetic hole

+Low time resolution plasma measurements

‡Plasma data contaminated by foreshock ions

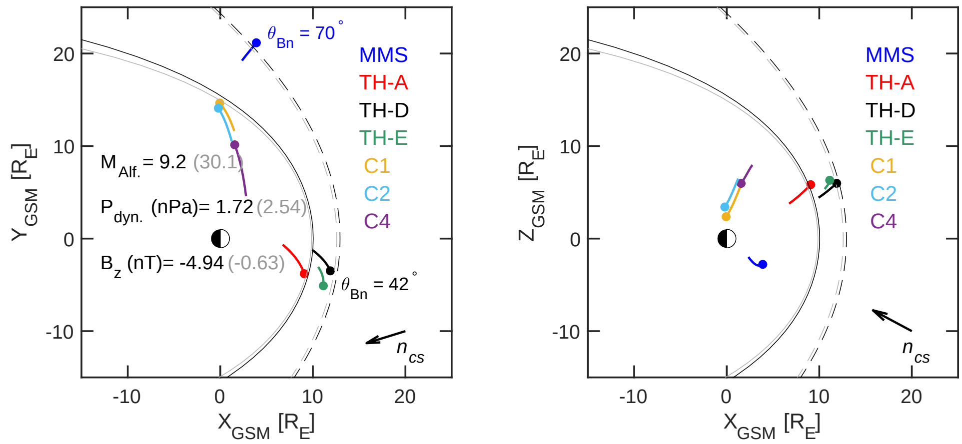

Figure 2. Spacecraft positions projected on the XY (left) and XZ (right) planes of GSM coordinates. THA is shown in red, THD in black, THE in green, Cluster1 (C1) in yellow, Cluster2 (C2) in cyan, and Cluster4 (C4) in purple. Trajectories are shown for a 3-hour interval between 09:30:00 and 12:30:00 UT on 20 November 2018. Tiny filled circles mark the beginning of the interval. The dashed parabolas represent the bow shock boundary modeled after Farris and Russell (1994), while the solid parabolas are the modeled magnetopause boundary (Shue et al., 1998). The grey boundaries are model prediction under upstream conditions inside the magnetic depression of the RCS. Model parameters are annotated on the left panel. The normal vector to the RCS plane (n_{cs}) is marked on the lower right corner of each panel. The shock angles (θ_{Bn}) correspond to the IMF orientation before the event onset at MMS and THD.

they are comparable in strength to changes due to reconnection exhausts within the RCS (see Figure 1.c–e).

As the bow shock recedes, MMS crosses a shock formed against the magnetic hole plasma. Inside the magnetic hole, the shock obliquity decreases but it remains in the quasi-perpendicular regime ($\theta_{Bn} \sim 56°$). The low magnetic energy density and increased plasma density within the magnetic hole result in a high β and low Alfvén speed in the solar wind plasma upstream of the shock. Plasma β and local Alfvén speeds are listed in Table 1. Precursor whistler waves are suppressed during this shock crossing. Instead, we observe high amplitude quasiperiodic magnetic pulsations with a period of 2 s in the spacecraft frame. We should also note regarding Table 1 that for events inside the magnetosheath the start time (t_i) is when the clock angle reaches the minimum ($\sim 170°$) inside the magnetic hole. This is because in the sheath plasma the magnetic field rotation at the leading edge of the RCS occurs over a longer time period than the solar wind. Plus, not all components undergo rotation at the same time or rate, which makes selecting an exact start time difficult and rather arbitrary.

During this time, THD is near the nose of the bow shock and in the foreshock region of the quasi-parallel side of the shock. THD magnetic field data are from the flux gate magnetometers (Auster et al., 2008), and plasma data are from the electrostatic analyzers (McFadden et al., 2008), and the solid state telescopes. Before the field rotation, THD measures high levels of turbulence (Figure 3.e). A significant population of suprathermal foreshock ions exists in this region, which excite these waves through the ion cyclotron instability. Rotation of the field at ~09:33:08 UT results in a traveling foreshock (Kajdič et al., 2014), and disappearance of waves. The shock angle inside the magnetic hole and immediately after the field rotation is about 72° and it mostly remains above 45° throughout the magnetic hole. The clock angle changes from ~280° to 168°, while the cone an-

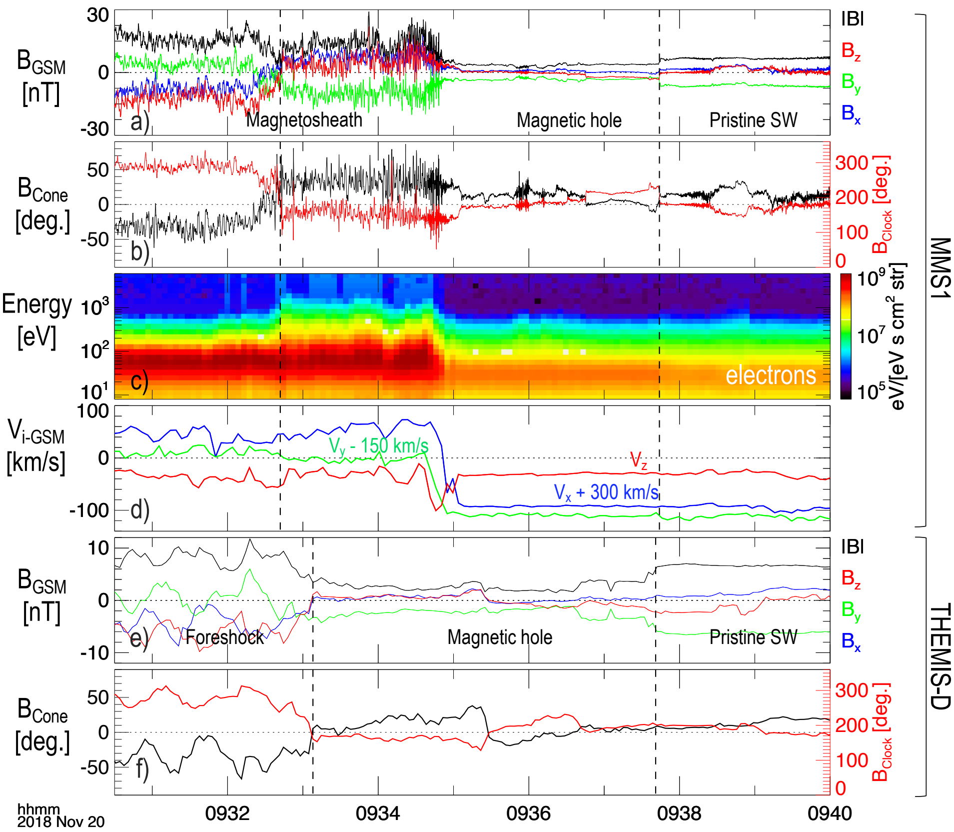

Figure 3. MMS1 and THD observations of the RCS and the SWMH crossing the bow shock. Panels (a–d) show MMS1 measurements near dusk side flank of the magnetic field components and magnitude, magnetic field cone and clock angles, electron energy spectrogram, and components of the ion bulk flow velocity, respectively. The vertical dashed lines on these panels indicate the boundaries of the SWMH as observed by MMS1. The spacecraft is initially in the magnetosheath. The V_x and V_y velocity components in panel (d) are shifted by +300 kms^{-3} and -150 kms^{-3}, respectively. Panels (e) and (f) show the magnetic field, and cone and clock angle data from THD spacecraft positioned near the nose of the bow shock. The vertical dashed lines mark the boundaries of the SWMH as observed by THD.

gle changes from -32° to ∼12°. THE is about 0.7 R_E downstream of THD and very close to the bow shock but still in the foreshock region. Its observations (not shown) are similar to THD except that foreshock structures at THE are much more intense with sporadic high amplitude steepened waves, and density of backstreaming ions is also higher at THE. The structure is observed by THE 16 s after THD (as indicated by t_i times in Table 1)) corresponding to an average radial solar wind flow speed of 292.8 kms^{-1}. This solar wind slowdown is due to foreshock effects that can begin much farther upstream of the shock beyond THD position, because backstreaming ions can travel long distances upstream along the magnetic field (Eastwood et al., 2005).

2.3 Changes in the magnetosheath and at the magnetopause

It has been shown that solar wind magnetic holes can bypass the bow shock and travel through the magnetosheath in the form of diamagnetic plasmoids (Karlsson et al., 2015). In Figure 3 we showed that the characteristic field rotation across the RCS in the solar wind can be clearly identified in magnetosheath plasma immediately downstream of the quasi-perpendicular bow shock in MMS data. During this event, THA is located at (9.0, -3.7, 5.8) R_E in the magnetosheath and downstream of the quasi-parallel side of the bow shock (see the shock angle map in Figure S2 in Supplementary Information section). Figure 4.a shows magnetic field cone and clock angles measured by THA, while the magnetic field components and strength are shown in panel (b). Before the structure arrives at THA, the B_x component of the magnetic field in the sheath plasma is pointing sunward, resulting in a positive cone angle of 14.5°. This B_x reversal at THA is due to sheath plasma draping around the magnetosphere (Coleman, 2005; Spreiter et al., 1966). The clock angle at the leading edge of the structure changes from 264° to 166° similar to changes observed at THD and MMS. The field rotation extends over a longer period and not all three components of the field undergo reversal at the same rate. Foreshock effects cause noticeable slowdown of the solar wind on the leading edge of the magnetic hole compared to the trailing edge. As such, the structure's trailing edge is processed through the shock faster than the leading edge. δB at THA is about 0.70, although at times the magnetic field strength is half of the IMF strength. The level of plasma turbulence inside the magnetic hole also decreases significantly compared to the surrounding magnetosheath. Several sporadic magnetic peaks are observed inside the magnetic hole that are linearly polarized and are accompanied by earthward directed transverse electron jets. Ions do not seem to be affected, which indicates that peaks are on electron kinetic scales. The magnetic peaks also seem to be unrelated to mirror mode waves as they lack any electron density enhancements. Yao et al. (2017) showed that these peaks tend to propagate in the background ion plasma rest frame, though their generation mechanism remains unexplained.

Figure 4.d shows that inside the magnetic hole, electrons have a broadened energy distribution extended over the 10-250 eV energy range. Some electrons are also accelerated to up to 4 keV. Acceleration and broadening are restricted to the magnetic hole and are more pronounced near its center, and are likely remnants of heating and acceleration of electrons during the shock crossing, rather than being generated at a nearby magnetopause reconnection zone (Phan et al., 2011). However, lack of exhaust ion jets in THA data does not support proximity to a reconnection zone. The electron temperature inside the magnetic hole is isotropic, and the average electron temperature slightly reduces from the ambient magnetosheath plasma. The ion temperature in anisotropic, with higher temperatures perpendicular to the field. Both ion density and average temperature increase inside the magnetic hole. We show the pressure terms in Figure 4.e including the ion (electron) thermal pressure $P_{i(e)} = n_{i(e)} k_b T_{i(e)}$, where $n_{i(e)}$ and $T_{i(e)}$ are the density and average temperature of ions (electrons), and k_b is the Boltzmann constant. In addition, the magnetic pressure $P_B = |B|^2/2\mu_0$ (μ_0 = vacuum permeability) and the total pressure $P_{tot.} = P_i + P_e + P_B$ are also shown. The decrease in the magnetic pressure is compensated by an increase in the ion thermal pressure, so the structure remains roughly pressure balanced as it travels through the magnetosheath. $P_{dyn.}$ is also shown on this panel to emphasize that although there are no high-speed (ion) plasma jets, the dynamic pressure within the magnetic hole is significantly higher than the surrounding magnetosheath plasma, and at times it can be even higher than the half solar wind pressure threshold (horizontal dotted line).

Variations in the plasma dynamic pressure can have an influence on the shape of the magnetopause and its standoff distance. The upstream IMF variations can also dramatically change the magnetic field topology and reconnection zones at the magnetopause (Trattner et al., 2016, 2020).

We use a model to estimate the probable magnetic field topology at the magnetopause and calculate the maximum magnetic shear angle between the convected IMF and the geomagnetic field (Trattner et al., 2007). The model is based on convection of the solar wind through the magnetosheath, local geomagnetic field at the magnetopause,

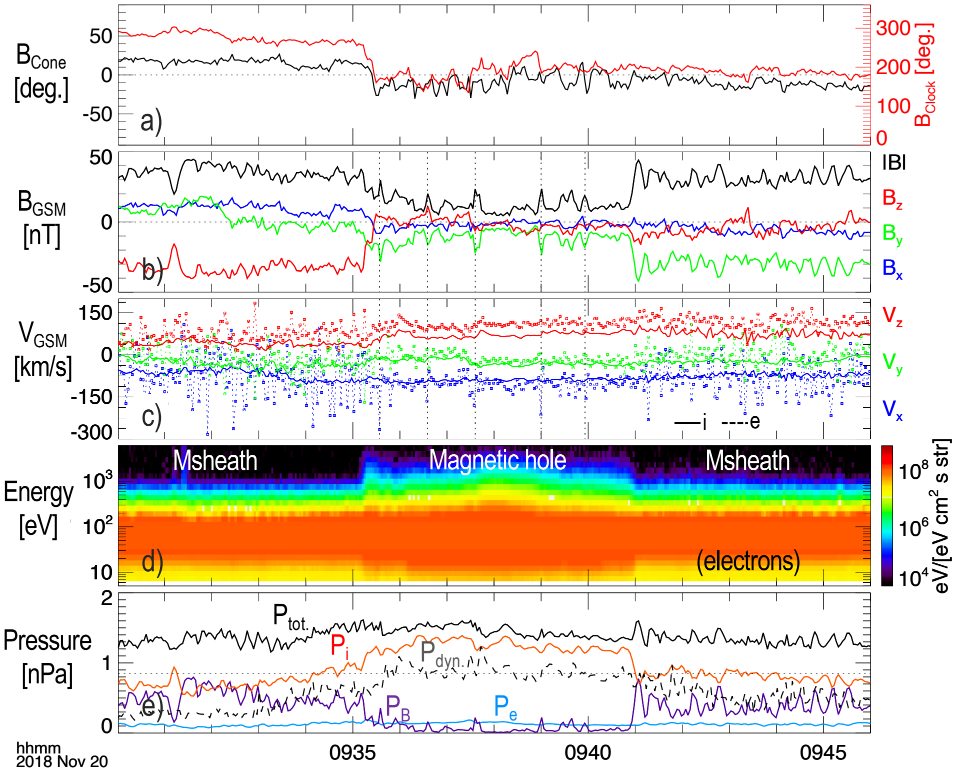

Figure 4. Observations of the RCS in the magnetosheath by THA. Panels show (a) the cone and clock angles, (b) magnetic field components and strength, (c) components of ion (solid lines) and electron (dotted lines) velocities, (d) electron energy spectrogram, and (e) pressure terms including, P_e: electron thermal pressure (blue), P_i: ion thermal pressure (red), P_B: magnetic pressure (purple), $P_{dyn.}$: dynamic pressure (grey-dotted), and total pressure $P_{tot.}$ (black). For reference, the horizontal dashed line in panel (e) is drawn at half the pristine solar wind dynamic pressure (0.85 nPa). Vertical dotted lines in panels (b–c) correspond to a select number of magnetic peaks inside the hole to emphasize the correspondence of these electron scale peaks to electron jets. Magnetosheath (Msheath) and magnetic hole intervals are identified on panel (d).

and draping effects. The model provides a first order approximation of the most probable regions across the magnetopause prone to reconnection. In Figure 5.a we show the maximum shear angle map at the magnetopause for solar wind conditions before the onset of the RCS when B_z is negative which creates high magnetic shear angles (red colors) along the Y–axis and mostly above the magnetic equatorial plane. The white streaks are regions with almost exactly anti-parallel field configuration. The shear angle map in Figure 5.b is generated based on plasma conditions within the magnetic hole where the dynamic pressure is high and after the magnetic field rotation the B_z component becomes very small. The white line connecting the two loci is the predicted location for the component reconnection line that extends more than 15 R_E across the magnetopause. THA, MMS1, and Cluster1 spacecraft positions are marked on both panels.

Another set of relevant observations are made by Cluster spacecraft that are inside the magnetopause boundary layer during this time. Cluster4 is close to the nose of the magnetopause, while Cluster1 and 2 are near the dusk flank, and downstream of the quasi-perpendicular side of the bow shock. Magnetic field measurements (Balogh et al., 2001) from Cluster1, 2, and 4 are shown in Figure 6. All three spacecraft observe tur-

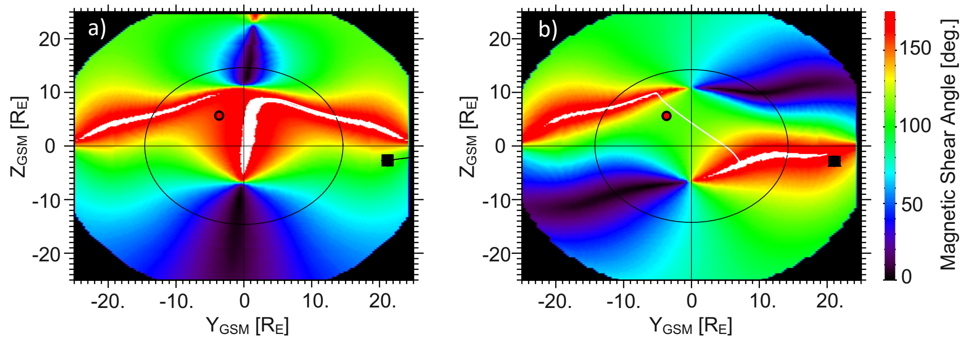

Figure 5. Maps of the magnetic shear angle between the convected IMF and the dipole field, and possible reconnection zones at the magnetopause. Each map shows a cross-sectional view of the magnetopause (black circle) viewed from the Sun. (a) The shear angle map at the magnetopause under convected solar wind conditions before the RCS onset (i.e., -B_z), (b) shear angles based on the solar wind conditions inside the magnetic hole. The white streaks are regions with almost exactly anti-parallel field configuration (within 3°). THA, MMS1, and Cluster1 spacecraft are also identified for reference.

bulence in the geomagnetic field between 09:35:00 and 09:40:00 UT, corresponding to the time when the solar wind RCS entered the magnetosheath. Magnetic perturbations seem to decrease with spacecraft distance to the magnetopause. Cluster1 is closest to the magnetopause boundary and records the highest magnetic perturbations, including B_z field reversals. The only source of -B_z at the position of Cluster1 inside the boundary layer is from the magnetosheath plasma and specifically from the period before the field rotation at the leading edge of the structure that we discussed. It seems that, after crossing the bow shock and travelling through the magnetosheath, the RCS impacts the magnetopause and forces the boundary inward. The last two panels in Figure 6 show normalized ion plasma flow velocities in the GSM XY (e) and XZ (f) planes. The plasma flow is highly turbulent in this region. We smoothed the velocity components over a 30 s interval to highlight the most intense variations. There are flow vertices at the position of Cluster4 throughout the period. Cluster4 also measures three plasma density peaks (not shown) at 09:36:34, 09:38:14, and 09:39:46 UT when the magnetospheric plasma density increases from ~ 0.7 cm^{-3} to 2.2, 2.9, and 2.0 cm^{-3}, respectively.

3 Discussion

We identified the event between 08:39:14 and 08:48:25 in Wind data as a reconnecting current sheet based on correlated/anti-correlated variations in By and V_y, enhancements in plasma density and temperature, high magnetic shear angle, and the absence of strahl electrons. Identifying and tracking this structure in other plasma environments is done through simultaneous observation of change in the magnetic field clock angle, magnetic field depression rate, and a relative increase in plasma density. These quantities are consistent between observations of the structure at different environments (see Table 1). However, it is evident from the measured magnetic field data in Figure 1 that there are other fine scale plasma structures evolving within this current sheet. The normal vector to the RCS plane at ACE is about 8° different than that at Wind. The event duration also increases from ACE to Wind, and then decreases at MMS near the bow shock. These differences can be due to the rotation of the RCS plane during transit between L1 and Earth's bow shock, or ongoing reconnection and plasma instabilities that modify the IMF.

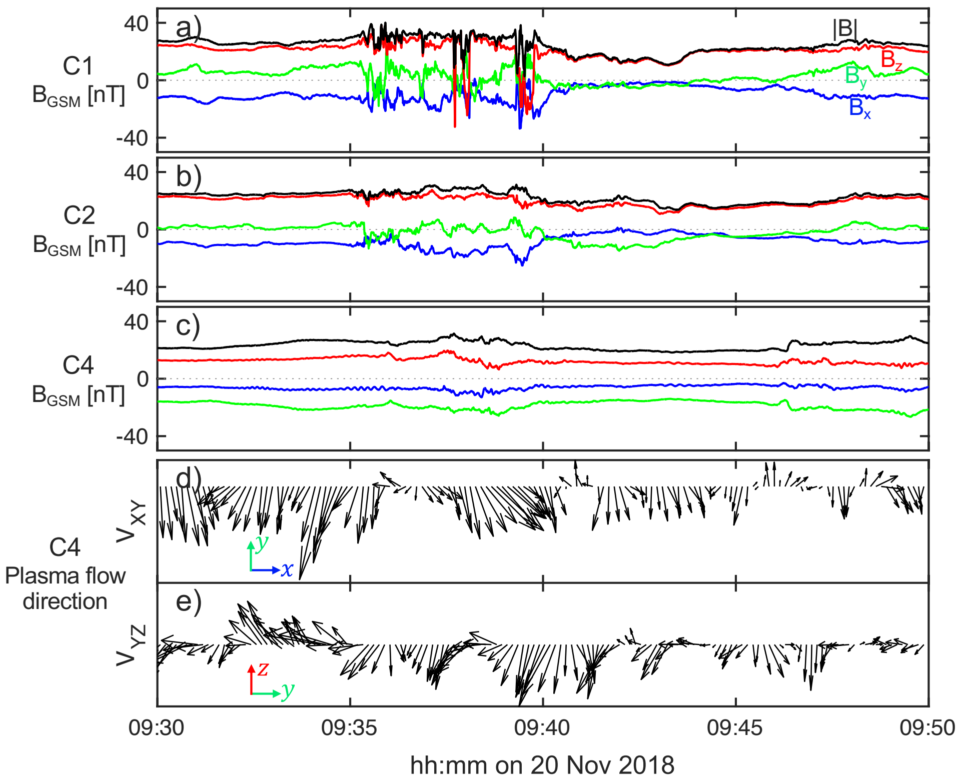

Figure 6. Cluster observations of the event inside the magnetosphere boundary layer. Panels (a – c) show the magnetic field data from Cluster1, 2, and 4, respectively. Panels d and e show normalized plasma velocities measured by Cluster4 in the GSM XY and YZ planes.

3.1 Asymmetric interaction

Even though MMS is 7.2 RE downstream of THD and in the magnetosheath, it observes the structure 24 s before THD, indicating that the RCS with high momentum plasma enters the magnetosheath through the flank region of the bow shock first and then the through subsolar region. This order of observations also agrees with the estimated orientation of RCS plane which hits the (+X, +Y, -Z) quadrant of the bow shock first. More important, before the magnetic hole arrival THD is upstream of the quasi-parallel side of the shock, where foreshock effects tend to significantly decelerate the solar wind. Backstreaming ions in the foreshock can travel far distances upstream of the shock along the magnetic field line and perturb the solar wind. As such, the upstream structures arrive at and cross the quasi-perpendicular side of the bow shock sooner than the quasi-parallel side (Turc et al., 2020). Regardless of the underlying cause, these asymmetric interactions across the bow shock will inevitably transfer downstream and create asymmetric interaction zones at the magnetopause boundary (Keika et al., 2009; Webster et al., 2021). As we showed in Figure 3 with MMS data, crossing the bow shock can also modify the exhaust flows within the RCS, which can disrupt any active ongoing reconnection (Phan et al., 2011). Survival of the reconnection jets across the bow shock is dependent on the direction of reconnection exhausts and the location of bow shock crossing, which can further contribute to creating variable plasma environments downstream of the bow shock. Reduced Alfvénic speed accompanied by increased plasma β within the magnetic hole and upstream of the bow shock have implications for generation of upstream instabilities (Madanian et al., 2021; Petrukovich & Chugunova, 2021).

3.2 Global impact

THD and MMS spacecraft are separated by more than 27 R_E across the bow shock, while THA and Cluster1 are separated by around 20 R_E across the magnetopause boundary. The fact that the same structure is seen by observers near the nose and flank regions of the bow shock indicates that the solar wind RCS plane covers most of the dayside bow shock surface. After crossing the bow shock and deflection of the solar wind plasma, THA located near the nose of the magnetopause and Cluster1 located near the dusk flank boundary layer record the passage of this structure which provide more evidence for the global scale of the RCS impact on the magnetosphere. Ion and electron velocities in Figure 4.c show that THA observes a draped plasma flow pointed mostly towards Earth and northward, consistent with the position of THA. At the leading edge of the magnetic hole, field rotation is accompanied by an increase in V_z, suggesting that flow deflection increases as the structure propagates through the magnetosheath. This flow pattern is consistent with our earlier observation of asymmetric encounter of the solar wind RCS plane with the bow shock, which can preferentially drive the magnetosheath plasma parallel to its normal vector. It should be noted that the V_z component of the ion velocity may have been affected by the spacecraft potential and the actual value may be higher and closer to that of electrons. The time delay between observing the structure at the nose of the bow shock in THE data, and later inside the magnetosheath near the magnetopause by THA is 126 s. An interesting point to note here is that the RCS crosses the bow shock and travels through the magnetosheath to regions close to the magnetopause boundary before the bow shock recedes behind MMS. THEMIS and MMS spacecraft travel at slow speeds (~ 1 kms^{-3}) during this period, significantly slower and almost stationary compared to the surrounding plasma flows that they measure.

3.3 Energy input and reconnection at the magnetopause

Although reconnection converts magnetic energy to plasma kinetic energy, at Earth's dayside magnetopause it is the upstream solar wind flow energy that is being dissipated through reconnection. When the solar wind IMF has already been depleted, for instance through reconnection within the solar wind, the dynamics of reconnection at the magnetopause can become more complicated. In Figure 3 and 4 we show that inside the magnetosheath the field rotation at the leading edge of the structure expands in time compared to its trailing edge. The change in the IMF direction also to some extent reduced the areas of high magnetic shear across the magnetopause (Figure 5.b). The plasma β inside the magnetic hole is higher than the surrounding magnetosheath plasma, and much higher than the low-density boundary layer plasma. These conditions seem to have adverse effects on the reconnection rate at the magnetopause. Without plasma data measured during magnetopause crossing, we cannot determine whether the B_z field reversals in Cluster1 data are accompanied by reconnection jets or whether they are simply "bulges" in the magnetopause boundary. On the other hand, Cluster2 that is very close to Cluster1 but farther from the modeled boundary did not detect any field reversals. This possible interplay between reconnection and magnetopause motion requires more investigations.

Previous simulation (Wu et al., 1993) and observation studies (Maynard et al., 2011) have suggested that under high β and low $|B|$ magnetosheath plasma, which is also the case in Figure 4.e, coupling between magnetosheath plasma to the low-latitude boundary layer is through hydrodynamic forcing, which ultimately causes an anti-Sunward convection at the high-latitude ionosphere. The ionospheric outflow data during this event measured by the Defense Meteorological Satellites Program (DMSP) satellite F18 did not corroborate this hypothesis. The spacecraft which crossed the northern polar cap at the time of these observations and we did not find any features in the ionospheric plasma drift data different than later orbits when the solar wind is calm. This may be due to the fact that the perturbations discussed are not strong or long enough to cause such an effect. Furthermore, as we showed in Figure 6, such perturbations are quickly weakened inside the magnetopause boundary within a short distance between Cluster1 and 2 (see Figure 6 and 2).

4 Conclusion

In this study we follow an RCS initially observed in the solar wind upstream of Earth at 1 AU to the bow shock, through the magnetosheath and to the magnetopause. Reconnection in the solar wind converts the IMF energy into plasma kinetic energy, thus depleting the magnetic field strength within the current sheet, while increasing the plasma density and temperature and creating a high momentum plasma layer. Rotational SWMHs associated with RCS are caused by magnetic reconnection and show noticeable enhancement in both plasma density and temperature. It has been shown that RCS can last over long distances (Phan et al., 2009). Once reconnection begins, there is infinite magnetic field energy available to the process. We show that the RCS enters the bow shock through the flank regions rather the subsolar point. Upon crossing with the bow shock, electron heating and acceleration are more efficient within the magnetically depleted layer, and accelerated electrons remain restricted to the magnetic hole inside the magnetosheath.

We show that the RCS plane covers a wide area across the dayside bow shock and magnetopause boundaries. The RCS and its SWMH form a high dynamic pressure plasma layer inside the magnetosheath. Given the global nature of the interaction, it would be a misnomer to categorize such a structure as a plasma jet, although it may very well fit some selection criteria of high speed jets (i.e., enhanced dynamic pressure above half the solar dynamic pressure). Nonetheless, similar to high-speed jets, RCS and their SWMHs can cause asymmetric deformation of the magnetopause boundary, and modulate the reconnection rate. The magnetosphere seems to act as a cushion against this high momentum layer, as the amplitude of perturbations decreases deeper inside the magnetosphere boundary layer (see Figure 6). Understanding the role of turbulence due to reconnection in creating magnetic depressions outside the RCS, and modulation of the reconnection process at the magnetopause due to these structures requires more analysis in future studies. Furthermore, the impact of RCS and their SWMH on planets without an intrinsic magnetosphere also deserves to be investigated.

Acknowledgments

We thank the mission operation and instrument teams on ACE, Wind, THEMIS, Cluster, and MMS missions for making their science data available. All data used in this study are publicly accessible through `https://spdf.gsfc.nasa.gov/pub/data/`. This work was partially supported by National Aeronautics and Space Administration (NASA) grant NNG04EB99C. The research at LASP was also supported in part by NASA grant 80NSSC20K0688. HM acknowledges the support from the ISSI team on magnetic holes.

References

Andreeova, K., Pulkkinen, T. I., Palmroth, M., & McPherron, R. (2011). Geoefficiency of solar wind discontinuities. *Journal of Atmospheric and Solar-Terrestrial Physics*, *73*(1), 112–122. doi: 10.1016/j.jastp.2010.03.006

Angelopoulos, V. (2008). The THEMIS mission. *Space Science Reviews*, *141*(1-4), 5–34. doi: 10.1007/s11214-008-9336-1

Archer, M. O., Horbury, T. S., & Eastwood, J. P. (2012, 5). Magnetosheath pressure pulses: Generation downstream of the bow shock from solar wind discontinuities. *Journal of Geophysical Research: Space Physics*, *117*(5). doi: 10.1029/2011JA017468

Auster, H. U., Glassmeier, K. H., Magnes, W., Aydogar, O., Baumjohann, W., Constantinescu, D., ... Wiedemann, M. (2008). The THEMIS flux-gate magnetometer. *Space Science Reviews*, *141*(1-4), 235–264. doi: 10.1007/s11214-008-9365-9

Balikhin, M. A., Sibeck, D. G., Runov, A., & Walker, S. N. (2012, 8). Magnetic holes in the vicinity of dipolarization fronts: Mirror or tearing structures? *Journal of Geophysical Research: Space Physics*, *117*(8). doi: 10.1029/2012JA017552

Balogh, A., Carr, C. M., Acuña, M. H., Dunlop, M. W., Beek, T. J., Brown, P., ... Schwingenschuh, K. (2001, 9). The Cluster Magnetic Field Investigation: overview of in-flight performance and initial results. *Annales Geophysicae*, *19*(10/12), 1207–1217. doi: 10.5194/angeo-19-1207-2001

Blanco-Cano, X., Preisser, L., Kajdič, P., & Rojas-Castillo, D. (2020). Magnetosheath Microstructure: Mirror Mode Waves and Jets during Southward IP Magnetic Field. *Journal of Geophysical Research: Space Physics*, *125*(9). doi: 10.1029/2020JA027940

Burch, J. L., Moore, T. E., Torbert, R. B., & Giles, B. L. (2016, 3). Magnetospheric Multiscale Overview and Science Objectives. *Space Science Reviews*, *199*(1-4), 5–21. doi: 10.1007/s11214-015-0164-9

Burlaga, L. F., Ness, N. F., & Acuna, M. H. (2007, 7). Linear magnetic holes in a unipolar region of the heliosheath observed by Voyager. *Journal of Geophysical Research: Space Physics*, *112*(7). doi: 10.1029/2007JA012292

Burlaga, L. F., Scudder, J. D., Klein, L. W., & Isenberg, P. A. (1990). Pressure-Balanced structures between 1 AU and 24 AU and their implications for solar wind electrons and interstellar pickup ions. *Journal of Geophysical Research*, *95*(A3), 2229. doi: 10.1029/ja095ia03p02229

Cassak, P. A., & Shay, M. A. (2007). Scaling of asymmetric magnetic reconnection: General theory and collisional simulations. *Physics of Plasmas*, *14*(10), 102114. doi: 10.1063/1.2795630

Coleman, I. J. (2005). A multi-spacecraft survey of magnetic field line draping in the dayside magnetosheath. *Annales Geophysicae*, *23*(3), 885–900. doi: 10.5194/angeo-23-885-2005

Drake, J. F., Swisdak, M., Opher, M., & Richardson, J. D. (2017). The Formation of Magnetic Depletions and Flux Annihilation Due to Reconnection in the Heliosheath. *The Astrophysical Journal*, *837*(2), 159. doi: 10.3847/1538-4357/aa6304

Eastwood, J. P., Lucek, E. A., Mazelle, C., Meziane, K., Narita, Y., Pickett, J., & Treumann, R. A. (2005, 6). The foreshock. *Space Science Reviews*, *118*(1-4), 41–94. doi: 10.1007/s11214-005-3824-3

Escoubet, C. P., Fehringer, M., & Goldstein, M. (2001, 9). The Cluster mission. *Annales Geophysicae*, *19*(10/12), 1197–1200. doi: 10.5194/angeo-19-1197-2001

Escoubet, C. P., Hwang, K. J., Toledo-Redondo, S., Turc, L., Haaland, S. E., Aunai, N., ... Torbert, R. B. (2020). Cluster and MMS Simultaneous Observations of Magnetosheath High Speed Jets and Their Impact on the Magnetopause. *Frontiers in Astronomy and Space Sciences*, *6*, 78. doi: 10.3389/fspas.2019.00078

Fairfield, D. H. (1974, 4). Whistler waves observed upstream from collisionless shocks. *Journal of Geophysical Research*, *79*(10), 1368–1378. doi: 10.1029/ja079i010p01368

Farris, M. H., & Russell, C. T. (1994). Determining the standoff distance of the bow shock: Mach number dependence and use of models. *Journal of Geophysical Research*, *99*(A9), 17681. doi: 10.1029/94ja01020

Farrugia, C. J., Erkaev, N. V., Biernat, H. K., & Burlaga, L. F. (1995). Anomalous magnetosheath properties during Earth passage of an interplanetary magnetic cloud. *Journal of Geophysical Research*, *100*(A10), 19245. doi: 10.1029/95ja01080

Gosling, J. T. (2012). Magnetic reconnection in the solar wind. *Space Science Reviews*, *172*(1-4), 187–200. doi: 10.1007/s11214-011-9747-2

Gosling, J. T., Skoug, R. M., McComas, D. J., & Smith, C. W. (2005). Direct evidence for magnetic reconnection in the solar wind near 1 AU. *Journal of Geophysical Research: Space Physics*, *110*(A1), A01107. doi: 10.1029/2004JA010809

Gosling, J. T., & Szabo, A. (2008). Bifurcated current sheets produced by magnetic reconnection in the solar wind. *Journal of Geophysical Research: Space Physics*, *113*(10). doi: 10.1029/2008JA013473

Hamrin, M., Gunell, H., Goncharov, O., De Spiegeleer, A., Fuselier, S., Mukherjee, J., … Giles, B. (2019). Can Reconnection be Triggered as a Solar Wind Directional Discontinuity Crosses the Bow Shock? A Case of Asymmetric Reconnection. *Journal of Geophysical Research: Space Physics*, *124*(11), 8507–8523. doi: 10.1029/2019JA027006

Harten, R., & Clark, K. (1995, 2). The design features of the GGS wind and polar spacecraft. *Space Science Reviews*, *71*(1-4), 23–40. doi: 10.1007/BF00751324

Hesse, M., & Cassak, P. A. (2020). Magnetic Reconnection in the Space Sciences: Past, Present, and Future. *Journal of Geophysical Research: Space Physics*, *125*(2). doi: 10.1029/2018ja025935

Hietala, H., Phan, T. D., Angelopoulos, V., Oieroset, M., Archer, M. O., Karlsson, T., & Plaschke, F. (2018). In Situ Observations of a Magnetosheath High-Speed Jet Triggering Magnetopause Reconnection. *Geophysical Research Letters*, *45*(4), 1732–1740. doi: 10.1002/2017GL076525

Hietala, H., & Plaschke, F. (2013). On the generation of magnetosheath high-speed jets by bow shock ripples. *Journal of Geophysical Research: Space Physics*, *118*(11), 7237–7245. doi: 10.1002/2013JA019172

Kahler, S., & Lin, R. P. (1994). The determination of interplanetary magnetic field polarities around sector boundaries using E ¿ 2 keV electrons. *Geophysical Research Letters*, *21*(15), 1575–1578. Retrieved from `http://doi.wiley.com/10.1029/94GL01362` doi: 10.1029/94GL01362

Kajdič, P., Lavraud, B., Zaslavsky, A., Blanco-Cano, X., Sauvaud, J. A., Opitz, A., … Luhmann, J. G. (2014, 9). Ninety degrees pitch angle enhancements of suprathermal electrons associated with interplanetary shocks. *Journal of Geophysical Research: Space Physics*, *119*(9), 7038–7060. doi: 10.1002/2014JA020213

Karlsson, T., Heyner, D., Volwerk, M., Morooka, M., Plaschke, F., Goetz, C., & Hadid, L. (2021). Magnetic Holes in the Solar Wind and Magnetosheath Near Mercury. *Journal of Geophysical Research: Space Physics*, *126*(5). doi: 10.1029/2020JA028961

Karlsson, T., Kullen, A., Liljeblad, E., Brenning, N., Nilsson, H., Gunell, H., & Hamrin, M. (2015, 9). On the origin of magnetosheath plasmoids and their relation to magnetosheath jets. *Journal of Geophysical Research A: Space Physics*, *120*(9), 7390–7403. doi: 10.1002/2015JA021487

Karlsson, T., Liljeblad, E., Kullen, A., Raines, J. M., Slavin, J. A., & Sundberg, T. (2016, 9). Isolated magnetic field structures in Mercury's magnetosheath as possible analogues for terrestrial magnetosheath plasmoids and jets. *Planetary and Space Science*, *129*, 61–73. doi: 10.1016/j.pss.2016.06.002

Keika, K., Nakamura, R., Baumjohann, W., Angelopoulos, V., Kabin, K., Glassmeier, K. H., … Rankin, R. (2009). Deformation and evolution of solar wind discontinuities through their interactions with the Earths bow shock. *Journal of Geophysical Research: Space Physics*, *114*(9), n/a–n/a. doi: 10.1029/2008JA013481

Khotyaintsev, Y. V., Graham, D. B., Norgren, C., & Vaivads, A. (2019). Collisionless Magnetic Reconnection and Waves: Progress Review. *Frontiers in Astronomy and Space Sciences*, *6*, 70. doi: 10.3389/fspas.2019.00070

Kropotina, J. A., Webster, L., Artemyev, A. V., Bykov, A. M., Vainchtein, D. L., & Vasko, I. Y. (2021). Solar Wind Discontinuity Transformation at the Bow Shock. *The Astrophysical Journal*, *913*(2), 142. doi: 10.3847/1538-4357/abf6c7

Liemohn, M. W., & Welling, D. T. (2016, 10). Ionospheric and Solar Wind Contributions to Magnetospheric Ion Density and Temperature throughout the Magnetotail. In C. R. Chappell, R. W. Schunk, P. M. Banks, J. L. Burch, & R. M. Thorne (Eds.), *Geophysical monograph series* (pp. 101–114). Hoboken, NJ, USA: John Wiley & Sons, Inc. doi: 10.1002/9781119066880.ch8

Lin, Y. (1997, 11). Generation of anomalous flows near the bow shock by its interaction with interplanetary discontinuities. *Journal of Geophysical Research: Space Physics*, *102*(A11), 24265–24281. doi: 10.1029/97JA01989

Madanian, H., Desai, M. I., Schwartz, S. J., Wilson, L. B., Fuselier, S. A., Burch, J. L., ... Lindqvist, P.-A. (2021, 2). The Dynamics of a High Mach Number Quasi-perpendicular Shock: MMS Observations. *The Astrophysical Journal*, *908*(1), 40. doi: 10.3847/1538-4357/abcb88

Madanian, H., Halekas, J. S., Mazelle, C. X., Omidi, N., Espley, J. R., Mitchell, D. L., & McFadden, J. P. (2020, 12). Magnetic Holes Upstream of the Martian Bow Shock: MAVEN Observations. *Journal of Geophysical Research: Space Physics*, *125*(1). doi: 10.1029/2019JA027198

Maynard, N. C., Farrugia, C. J., Burke, W. J., Ober, D. M., Scudder, J. D., Mozer, F. S., ... Siebert, K. D. (2011). Interactions of the heliospheric current and plasma sheets with the bow shock: Cluster and Polar observations in the magnetosheath. *Journal of Geophysical Research: Space Physics*, *116*(1), n/a–n/a. doi: 10.1029/2010JA015872

Maynard, N. C., Farrugia, C. J., Ober, D. M., Burke, W. J., Dunlop, M., Mozer, F. S., ... Siebert, K. D. (2008). Cluster observations of fast shocks in the magnetosheath launched as a tangential discontinuity with a pressure increase crossed the bow shock. *Journal of Geophysical Research: Space Physics*, *113*(10). doi: 10.1029/2008JA013121

McFadden, J. P., Carlson, C. W., Larson, D., Ludlam, M., Abiad, R., Elliott, B., ... Angelopoulos, V. (2008). The THEMIS ESA plasma instrument and in-flight calibration. *Space Science Reviews*, *141*(1-4), 277–302. doi: 10.1007/s11214-008-9440-2

Osman, K. T., Matthaeus, W. H., Gosling, J. T., Greco, A., Servidio, S., Hnat, B., ... Phan, T. D. (2014). Magnetic reconnection and intermittent turbulence in the solar wind. *Physical Review Letters*, *112*(21), 215002. doi: 10.1103/PhysRevLett.112.215002

Parker, E. N. (1957). Sweet's mechanism for merging magnetic fields in conducting fluids. *Journal of Geophysical Research*, *62*(4), 509–520. doi: 10.1029/jz062i004p00509

Paschmann, G., Haerendel, G., Papamastorakis, I., Sckopke, N., Bame, S. J., Gosling, J. T., & Russell, C. T. (1982). Plasma and magnetic field characteristics of magnetic flux transfer events. *Journal of Geophysical Research*, *87*(A4), 2159. doi: 10.1029/JA087iA04p02159

Paschmann, G., Øieroset, M., & Phan, T. (2013, 10). In-Situ Observations of Reconnection in Space. *Space Science Reviews*, *178*(2-4), 385–417. doi: 10.1007/s11214-012-9957-2

Petrukovich, A. A., & Chugunova, O. M. (2021). Detailed Structure of Very High-β Earth Bow Shock. *Journal of Geophysical Research: Space Physics*, *126*(8). doi: 10.1029/2020JA029004

Petschek, H. E. (1964). Magnetic Field Annihilation. *The Physics of Solar Flares, Proceedings of the AAS-NASA Symposium*, *50*, 425.

Phan, T. D., Gosling, J. T., & Davis, M. S. (2009). Prevalence of extended reconnection X-lines in the solar wind at 1 AU. *Geophysical Research Letters*, *36*(9), L09108. doi: 10.1029/2009GL037713

Phan, T. D., Gosling, J. T., Davis, M. S., Skoug, R. M., Øieroset, M., Lin, R. P., … Balogh, A. (2006). A magnetic reconnection X-line extending more than 390 Earth radii in the solar wind. *Nature*, *439*(7073), 175–178. doi: 10.1038/nature04393

Phan, T. D., Gosling, J. T., Paschmann, G., Pasma, C., Drake, J. F., Øieroset, M., … Davis, M. S. (2010). The dependence of magnetic reconnection on plasma β and magnetic shear: Evidence from solar wind observations. *Astrophysical Journal Letters*, *719*(2 PART 2), L199–L203. doi: 10.1088/2041-8205/719/2/L199

Phan, T. D., Love, T. E., Gosling, J. T., Paschmann, G., Eastwood, J. P., Oieroset, M., … Auster, U. (2011). Triggering of magnetic reconnection in a magnetosheath current sheet due to compression against the magnetopause. *Geophysical Research Letters*, *38*(17). doi: 10.1029/2011GL048586

Phan, T. D., Paschmann, G., Twitty, C., Mozer, F. S., Gosling, J. T., Eastwood, J. P., … Lucek, E. A. (2007, 7). Evidence for magnetic reconnection initiated in the magnetosheath. *Geophysical Research Letters*, *34*(14), L14104. doi: 10.1029/2007GL030343

Plaschke, F., Hietala, H., & Angelopoulos, V. (2013). Anti-sunward high-speed jets in the subsolar magnetosheath. *Annales Geophysicae*, *31*(10), 1877–1889. doi: 10.5194/angeo-31-1877-2013

Pollock, C., Moore, T., Jacques, A., Burch, J., Gliese, U., Saito, Y., … Zeuch, M. (2016, 3). Fast Plasma Investigation for Magnetospheric Multiscale. *Space Science Reviews*, *199*(1-4), 331–406. doi: 10.1007/s11214-016-0245-4

Russell, C. T., Anderson, B. J., Baumjohann, W., Bromund, K. R., Dearborn, D., Fischer, D., … Richter, I. (2016, 3). *The Magnetospheric Multiscale Magnetometers* (Vol. 199) (No. 1-4). Springer Netherlands. doi: 10.1007/s11214-014-0057-3

Šafránková, J., Němeček, Z., Přech, L., Samsonov, A. A., Koval, A., & Andréeová, K. (2007). Modification of interplanetary shocks near the bow shock and through the magnetosheath. *Journal of Geophysical Research: Space Physics*, *112*(8), n/a–n/a. doi: 10.1029/2007JA012503

Shue, J.-H., Song, P., Russell, C. T., Steinberg, J. T., Chao, J. K., Zastenker, G., … Kawano, H. (1998). Magnetopause location under extreme solar wind conditions. *Journal of Geophysical Research: Space Physics*, *103*(A8), 17691–17700. doi: 10.1029/98ja01103

Sperveslage, K., Neubauer, F. M., Baumgärtel, K., & Ness, N. F. (2000). Magnetic holes in the solar wind between 0.3 AU and 17 AU. *Nonlinear Processes in Geophysics*, *7*(3/4), 191–200. doi: 10.5194/npg-7-191-2000

Spreiter, J. R., Summers, A. L., & Alksne, A. Y. (1966). Hydromagnetic flow around the magnetosphere. *Planetary and Space Science*, *14*(3), 223–253. doi: 10.1016/0032-0633(66)90124-3

Stone, E. C., Frandsen, A. M., Mewaldt, R. A., Christian, E. R., Margolies, D., Ormes, J. F., & Snow, F. (1998). The advanced composition explorer. *Space Science Reviews*, *86*(1-4), 1–22. doi: 10.1007/978-94-011-4762-0{_}1

Trattner, K. J., Burch, J. L., Ergun, R., Fuselier, S. A., Gomez, R. G., Grimes, E. W., … Young, D. T. (2016). The response time of the magnetopause reconnection location to changes in the solar wind: MMS case study. *Geophysical Research Letters*, *43*(10), 4673–4682. doi: 10.1002/2016GL068554

Trattner, K. J., Burch, J. L., Fuselier, S. A., Petrinec, S. M., & Vines, S. K. (2020). The 18 November 2015 Magnetopause Crossing: The GEM Dayside Kinetic Challenge Event Observed by MMS/HPCA. *Journal of Geophysical Research: Space Physics*, *125*(7). doi: 10.1029/2019JA027617

Trattner, K. J., Mulcock, J. S., Petrinec, S. M., & Fuselier, S. A. (2007). Probing the boundary between antiparallel and component reconnection during southward interplanetary magnetic field conditions. *Journal of Geophysical Research: Space Physics*, *112*(8). doi: 10.1029/2007JA012270

Treumann, R. A., & Baumjohann, W. (2013). Collisionless magnetic reconnection in space plasmas. *Frontiers in Physics*, *1*. doi: 10.3389/fphy.2013.00031

Tsurutani, B. T., Lakhina, G. S., Verkhoglyadova, O. P., Echer, E., Guarnieri, F. L., Narita, Y., & Constantinescu, D. O. (2011, 2). Magnetosheath and heliosheath mirror mode structures, interplanetary magnetic decreases, and linear magnetic decreases: Differences and distinguishing features. *Journal of Geophysical Research: Space Physics*, *116*(2), n/a–n/a. doi: 10.1029/2010JA015913

Turc, L., Escoubet, C. P., Fontaine, D., Kilpua, E. K., & Enestam, S. (2016). Cone angle control of the interaction of magnetic clouds with the Earth's bow shock. *Geophysical Research Letters*, *43*(10), 4781–4789. doi: 10.1002/2016GL068818

Turc, L., Tarvus, V., Dimmock, A. P., Battarbee, M., Ganse, U., Johlander, A., ... Palmroth, M. (2020, 10). Asymmetries in the Earth's dayside magnetosheath: results from global hybrid-Vlasov simulations. *Annales Geophysicae*, *38*(5), 1045–1062. doi: 10.5194/angeo-38-1045-2020

Turner, J. M., Burlaga, L. F., Ness, N. F., & Lemaire, J. F. (1977, 5). Magnetic holes in the solar wind. *Journal of Geophysical Research*, *82*(13), 1921–1924. doi: 10.1029/ja082i013p01921

Volwerk, M., Mautner, D., Simon Wedlund, C., Goetz, C., Plaschke, F., Karlsson, T., ... Varsani, A. (2021). Statistical study of linear magnetic hole structures near Earth. *Annales Geophysicae*, *39*(1), 239–253. doi: 10.5194/angeo-39-239-2021

Wang, G. Q., Volwerk, M., Xiao, S. D., Wu, M. Y., Hao, Y. F., Liu, L. J., ... Zhang, T. L. (2020, 11). Three-dimensional Geometry of the Electron-scale Magnetic Hole in the Solar Wind. *The Astrophysical Journal Letters*, *904*(1), L11. doi: 10.3847/2041-8213/abc553

Webster, L., Vainchtein, D., & Artemyev, A. (2021). Solar Wind Discontinuity Interaction with the Bow Shock: Current Density Growth and Dawn-Dusk Asymmetry. *Solar Physics*, *296*(6), 87. doi: 10.1007/s11207-021-01824-2

Wu, B. H., Mandt, M. E., Lee, L. C., & Chao, J. K. (1993). Magnetospheric Response to Solar Wind Dynamic Pressure Variations: Interaction of Interplanetary Tangential Discontinuities with the Bow Shock. *Journal of Geophysical Research*, *98*(A12), 21297–21311. doi: 10.1029/93ja01013

Yamada, M., Kulsrud, R., & Ji, H. (2010). Magnetic reconnection. *Reviews of Modern Physics*, *82*(1), 603–664. doi: 10.1103/RevModPhys.82.603

Yao, S. T., Wang, X. G., Shi, Q. Q., Pitkänen, T., Hamrin, M., Yao, Z. H., ... Liu, J. (2017). Observations of kinetic-size magnetic holes in the magnetosheath. *Journal of Geophysical Research: Space Physics*, *122*(2), 1990–2000. doi: 10.1002/2016JA023858

Zhang, H., Zong, Q. G., Sibeck, D. G., Fritz, T. A., McFadden, J. P., Glassmeier, K. H., & Larson, D. (2009). Dynamic motion of the bow shock and the magnetopause observed by THEMIS spacecraft. *Journal of Geophysical Research: Space Physics*, *114*(1), n/a–n/a. doi: 10.1029/2008JA013488

Zweibel, E. G., & Yamada, M. (2016). Perspectives on magnetic reconnection. *Proceedings of the Royal Society A: Mathematical, Physical and Engineering Sciences*, *472*(2196), 20160479. doi: 10.1098/rspa.2016.0479

Supporting Information for "Asymmetric interaction of a solar wind reconnecting current sheet and its magnetic hole with Earth's bow shock and magnetosphere"

Hadi Madanian[1], Terry Z. Liu[2], Tai D. Phan[3], Karlheinz J. Trattner[4],

Tomas Karlsson[5], Michael W. Liemohn[6]

[1]Southwest Research Institute, San Antonio, TX, USA

[2]University of California Los Angeles, Los Angeles, CA, USA

[3]Space Sciences Laboratory, University of California, Berkeley, CA, USA

[4]Laboratory for Atmospheric and Space Sciences, Boulder, CO, USA

[5]KTH Royal Institute of Technology, Stockholm, Sweden

[6]Department of Climate and Space Sciences and Engineering, University of Michigan, Ann Arbor, MI, USA

Contents of this file

1. Figures S1 to S2

Additional Supporting Information (Files uploaded separately)

1. Captions for Figures S1 to S2

Figure S1. Minimum variance analysis results on ACE and Wind magnetic field data. Panels show (a and d) magnetic field strength, (b and e) magnetic field in GSM, (c and f) magnetic field components in the minimum variance coordinates. Details of the MVA output are annotated on panels (c) and (f).

Figure S2. Cross-section view of the shock angle. The IMF is chosen before the onset of the RCS. Positions of MMS1, THEMIS and Cluster spacecraft are also indicated.

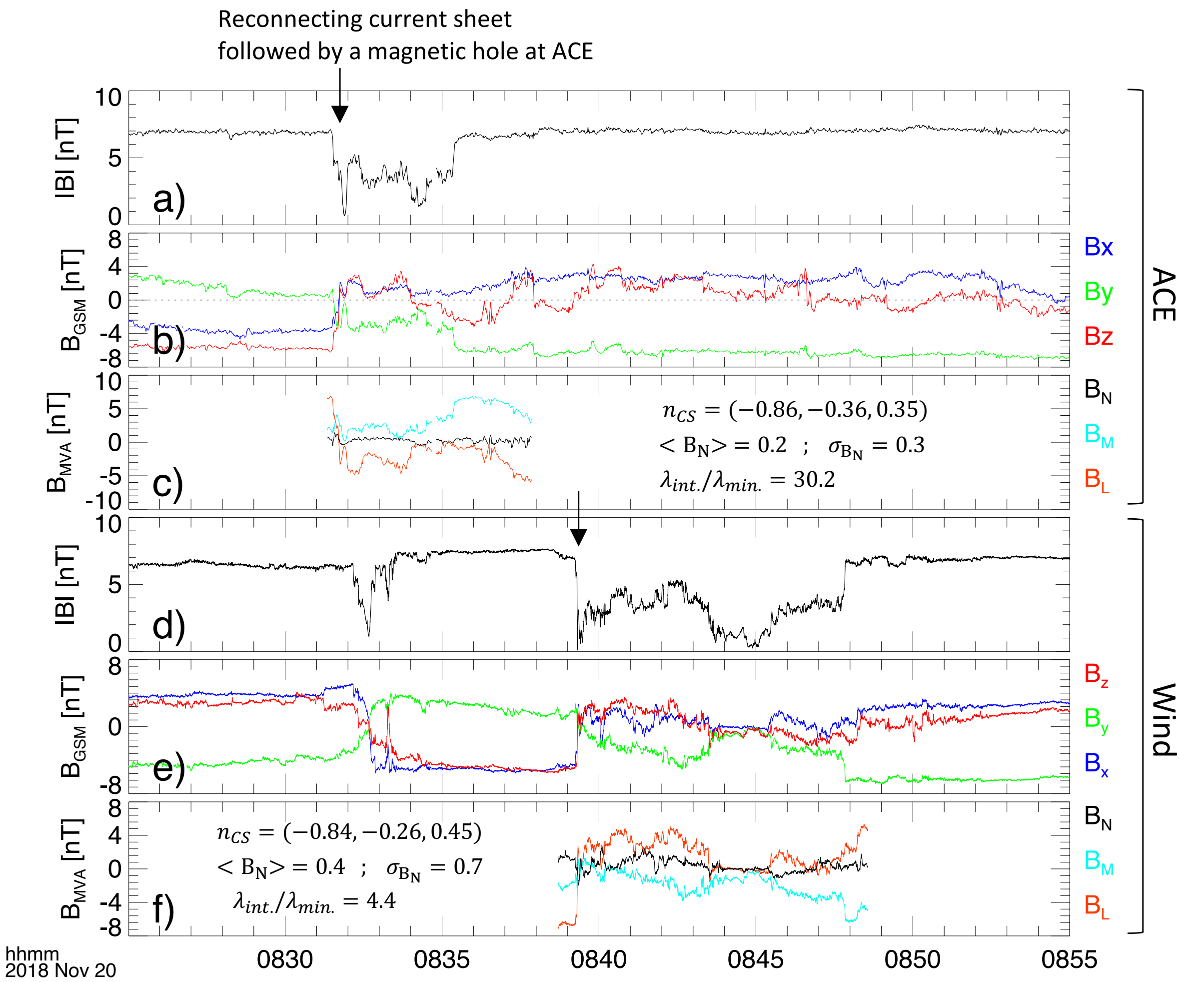

Figure S1. Minimum variance analysis results on ACE and Wind magnetic field data. Panels show (a and d) magnetic field strength, (b and e) magnetic field in GSM, (c and f) magnetic field components in the minimum variance coordinates. Details of the MVA output are annotated on panels (c) and (f).

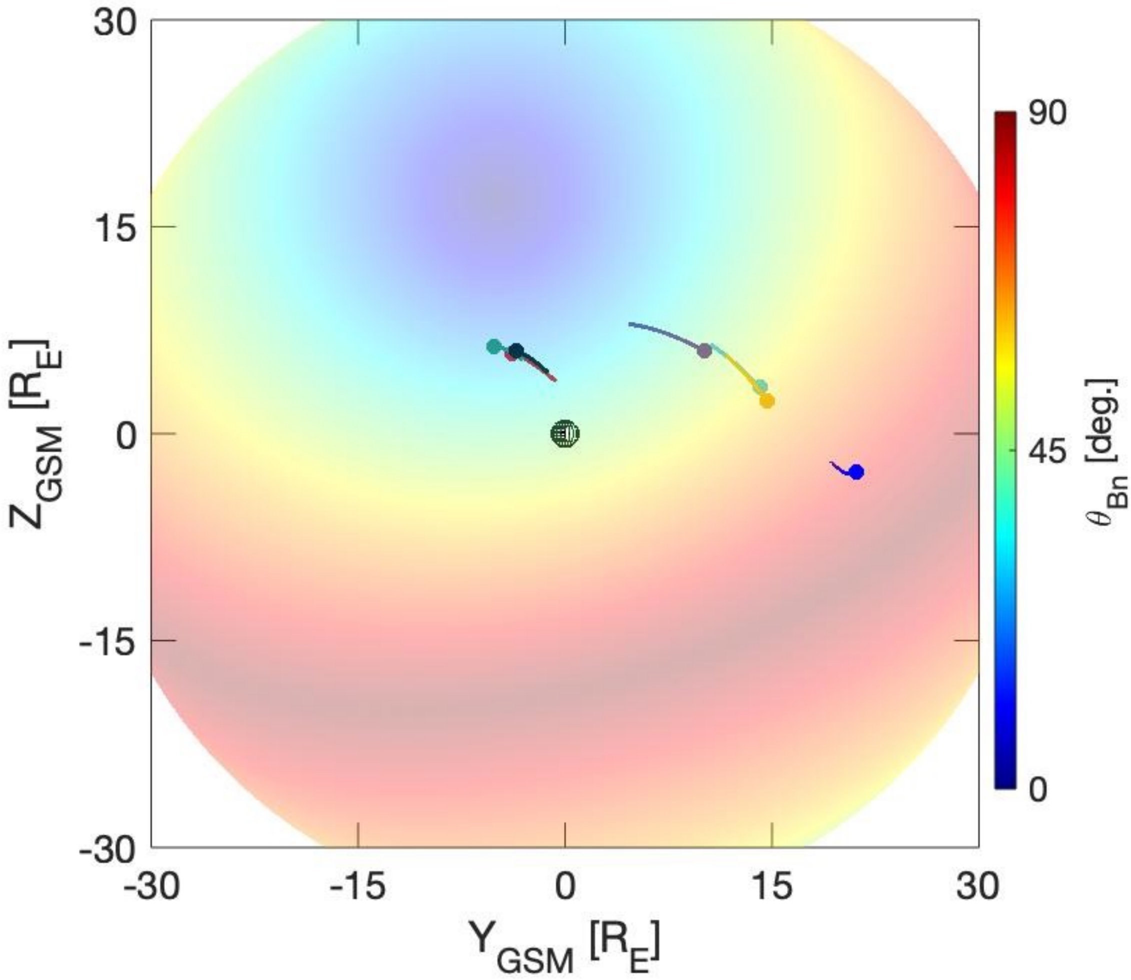

Figure S2. Cross-section view of the shock angle. The IMF is chosen before the onset of the RCS. Positions of MMS1, THEMIS and Cluster spacecraft are also indicated.